Materials Advances

ROYAL SOCIETY OF CHEMISTRY

PAPER

View Article Online
View Journal | View Issue

Cite this: *Mater. Adv.*, 2026, 7, 1291

Flexible donor–acceptor nanocomposite for triggered photocatalytic CO_2 fixation *via* an artificial leaf approach†

Kuldeep Kumar,[a] Rajesh K. Yadav,*[a] Rajesh K. Verma,*[b] Sanjay Mishra,[c] Kanchan Sharma,[a] Rehana Shahin,[a] Shaifali Mishra,[a] Satyam Singh,[a] Atul P. Singh,[f] Navneet K. Gupta[d] and Jin OoK Baeg*[e]

Mechanically triggered polymeric nanocomposites offer a promising solution for sustainable chemical recycling and minimize environmental pollution. In this study, a flexible, biodegradable donor–acceptor nanocomposite artificial leaf was synthesized as a photocatalyst by incorporating magnesium tetraphenyl-porphyrin (T) and aloe-vera-derived graphene (G) into polylactic acid (P) *via* the blown film method. This process yielded photocatalyst films with excellent mechanical properties, including ultra-high tensile strength, bending strength, impact strength, and surface hardness. The resulting film photocatalyst, PGT, was evaluated at three aloe-vera-derived graphene loadings (0.5%, 1%, and 1.5% G). Among these, the 1% PGT photocatalyst with an integrated donor–acceptor architecture incorporated into a nanocomposite artificial leaf as a film photocatalyst demonstrated the best performance, achieving significant levels of active 1,4-NADH regeneration (61.09 ± 0.59%) *via* solar light, which was efficiently used by the formate dehydrogenase enzyme to exclusively generate formic acid (HCOOH at approximately 146.62 ± 1.6 μmol) from CO_2. The PGT nanocomposite, with its extremely high tensile strength (25.322 MPa), tensile load (589.49 Newtons), strain (11.755%), bending strength (32.244 MPa), and impact energy (2.4615 J), can serve as a suitable material for tissue implants for various applications. The 1% PGT nanocomposite flexible artificial leaf as a film photocatalyst has a remarkable ability to fix CO_2 into HCOOH compared to the 0.5% and 1.5% PGT flexible film photocatalysts. Overall, the outcome demonstrates the potential and adaptability of these P-based nanocomposite artificial leaves (PGT), emphasizing their importance in photocatalysis, solar chemical synthesis, and scaffold-based tissue engineering.

Received 5th November 2024,
Accepted 24th June 2025

DOI: 10.1039/d4ma01103a

rsc.li/materials-advances

1. Introduction

During each respiratory cycle, 400–500 mL of air are inspired and exhaled by adults.[1] Notably, individuals spend approximately 90% of their time indoors—in homes, offices, shopping malls, gyms, and educational institutions.[2] With such prolonged indoor exposure, indoor air quality becomes a critical determinant of human health and overall well-being.[3] Poor indoor air quality, particularly due to microbial contaminants such as pathogenic bacteria[4] and airborne viruses such as the severe acute respiratory syndrome coronavirus 2 (SARS-CoV-2),[5–7] can pose significant health threats. The growing burden of air pollutants further exacerbates this issue. Airborne contaminants disturb the ecological equilibrium and also create favourable conditions for the growth and transmission of harmful pathogens. These pollutants include a diverse array of greenhouse gases such as methane, carbon dioxide (CO_2), nitrous oxide, perfluorocarbons, sulfur hexafluoride, and nitrogen trifluoride.[8]

Among all pollutants, anthropogenic CO_2 accounts for the main indoor and outdoor environmental problems, such as global warming,[8] carcinogenicity,[9] and adverse health effects.[10] One of the major issues that has surfaced in recent years is

[a] *Department of Chemistry and Environmental Science, Madan Mohan Malaviya University of Technology, Gorakhpur 273010, UP, India. E-mail: rajeshkr_yadav2003@yahoo.co.in*
[b] *Department of Mechanical Engineering, Harcourt Butler Technical University, Kanpur 208002, India. E-mail: rajeshverma.hbtu@gmail.com*
[c] *Department of Mechanical Engineering, Madan Mohan Malaviya University of Technology, Gorakhpur 273010, UP, India*
[d] *Centre for Sustainable Technologies, Indian Institute of Science, Bangalore Gulmohar Marg, Bengaluru 560012, India. E-mail: nkgupta@iisc.ac.in*
[e] *Korea Research Institute of Chemical Technology, 141 Gajeong-ro, Yuseong-gu, Daejeon, South Korea. E-mail: jobaeg@krict.re.kr*
[f] *Department of Chemistry, Central University, South Bihar, India*

† Electronic supplementary information (ESI) available. See DOI: https://doi.org/10.1039/d4ma01103a

global warming, largely brought about by an increase in the atmospheric level of carbon dioxide (CO_2).[1–4] Every day, a significant amount of CO_2 is emitted into the atmosphere through a variety of processes, notably by the burning of fossil fuels. Reliance on fossil fuels disrupts the carbon cycle and increases the excessive consumption of natural resources.[5,11,12]

Plants convert CO_2 into sugars through photosynthesis, playing a vital role in maintaining the global carbon cycle. However, excessive fossil fuel use, industrialization, deforestation, and urbanization have significantly disrupted this balance.[8–10] If anthropogenic CO_2 levels reach approximately 590 ppm, it has been projected that global temperatures will rise by 1.9 °C by 2100, with the polar regions warming nearly three times faster than the global average. In response, many countries are investing in sustainable and renewable energy technologies.[5,13] Recent scientific focus has shifted toward CO_2 capture, storage, and utilization (CCSU).[8–10,15–21] However, challenges such as high energy demands, complex system designs, and potential CO_2 leakage limit the practicality of the current CCS methods[8–10,14–21] The primary practical limitations of these techniques are the potential for CO_2 leakage, high energy requirements, and intricate designs.[5] Therefore, recycling or converting CO_2 into fuels and other goods with added value is a desirable way to alleviate the energy crisis and global warming without hindering urbanization and development.

CO_2 conversion is scientifically challenging, various strategies have been explored, including photocatalysis,[22–26] thermocatalysis,[27–31] radiolysis,[32–34] and biochemical conversion methods.[35,36] Among these, photocatalysis has been shown to be the most effective method, and involves using solar light irradiation to convert CO_2 into specific gaseous and liquid products, particularly for liquid products at ambient temperature and pressure.[37–39] Because this technology replicates the natural energy cycle, it is also known as artificial photosynthesis.[40]

In addition to using sustainable solar energy, flexible artificial leaf photocatalysis (FALPC) offers other important advantages, including control over product selectivity, environmental compatibility, and economic viability.[41–43] The conversion reaction of CO_2, a linear, chemically stable molecule with low electron affinity, is driven by nucleophilic attacks on the carbon atom.[44] More than 750 kJ mol^{-1} of energy is required for the dissociation of C=O bond.[45] As this process is thermodynamically uphill, additional energy is needed to dissociate the C=O bond, overcome resistance loss, and create band bending.[46]

Natural photosynthesis uses energy absorbed from sunlight using light harvesters/photosensitizers to accomplish thermodynamically uphill reactions, and our designed artificial photosynthetic route is similar in that it also enables reactions with a negative free energy change. For effective CO_2 conversion, the photogenerated electrons and holes must possess energy levels more negative and more positive, respectively, than the redox potentials of CO_2/HCOOH (−0.61 V) and H_2O/O_2 (0.82 V) at neutral pH.[37,47,48] Photocatalysts with a broad energy gap of 2.88 eV are required to execute redox processes, such as sacrificial agent oxidation and CO_2 fixation.[49] The amount of CO_2 transformation varies depending upon the various reported photocatalytic materials,[50] all of which exhibit weaker photocatalytic characteristics.[51]

This study presents the successful synthesis of a bendable, highly efficient light-harvesting nanocomposite with ultra-high tensile strength, high impact strength, and high surface hardness, for use as a flexible artificial leaf photocatalyst for CO_2 fixation using solar energy. The high tensile strength (25.322 MPa), tensile load (589.49 Newtons), strain (11.755%), bending strength (32.244 MPa), and impact energy (2.4615 Joules) of the PGT nanocomposite enable the material to participate in potential applications in tissue implants. The mechanical robustness of the nanocomposite plays a crucial role not only in structural durability and long-term usability but also in enhancing the photocatalytic performance by preserving the morphological integrity of the material during operation.

From a materials science perspective, tuning mechanical parameters such as flexibility, elasticity, and fracture resistance can enhance the photocatalytic activity by maintaining consistent surface area exposure, minimizing photocatalyst fatigue, and enabling conformal contact in real-world applications. In this context, the mechanical resilience of PGT nanocomposite ensures sustained light absorption and active site availability, which are critical for achieving efficient CO_2 conversion.[52–55]

We employed 0.5, 1, and 1.5% PGT nanocomposites to create flexible artificial leaves. In addition to simple and cost-effective preparation, the 'T' system exhibits an efficient energy-transfer ability, a high molar extinction coefficient, a long excited-state lifetime, and photochemical stability.[51–53] Scheme 1 illustrates a representation of a donor–acceptor 1% PGT nanocomposite-based flexible film, designed to function as an artificial leaf photocatalyst for environmental remediation applications, particularly the conversion of CO_2 into value-added solar chemicals. The donor–acceptor architecture facilitates efficient charge separation and transport, enhancing the overall photocatalytic efficiency under solar irradiation.

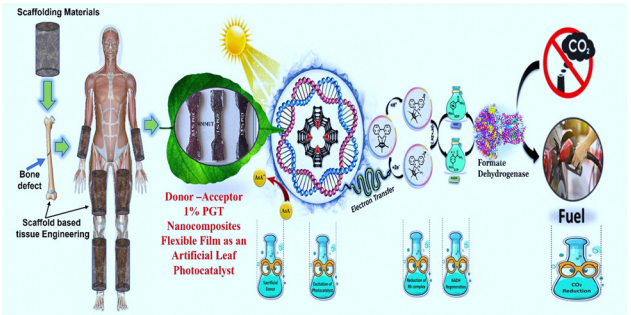

Scheme 1 Schematic representation of the donor–acceptor 1% PGT nanocomposite flexible film as an artificial leaf photocatalyst that will contribute to a clean environment, *e.g.*, by CO_2 fixation into value-added solar chemicals. Donor–acceptor flexible film scaffolding materials composed of 1% PGT nanocomposites are crucial for tissue engineering because they provide cells with the structural and physical support they need to connect, proliferate, and differentiate. This material can be used in regenerative medicine applications by creating and engineering it to imitate the natural tissue environment, which thus encourages the development of functional tissues and organs.

These flexible film scaffolds, composed of 1% PGT nanocomposites, also hold significance beyond photocatalysis. Their tunable physicochemical and mechanical properties provide a suitable microenvironment for cellular adhesion, proliferation, and differentiation, and therefore, they are promising candidates for tissue engineering and regenerative medicine. By mimicking the extracellular matrix, the nanocomposite scaffolds can support the development of functional tissues and organs, demonstrating their multifunctional utility in clean energy and biomedical domains. The resultant PGT nanocomposite flexible artificial leaf photocatalyst obtained by the blown film method exhibited superior performance due to ultra-high tensile and bending strength over the 0.5 and 1.5% PGT nanocomposite flexible artificial leaf photocatalysts in the regeneration of 1,4-NADH and exclusive formation of formic acid (HCOOH) from CO_2, enzymatically, using solar light.[56–59]

2. Results and discussion

2.1. Solar-powered formic acid production using photocatalysts and biocatalysts

The PGT nanocomposite photocatalyst, when integrated with a biological enzyme, *i.e.*, formate dehydrogenase, exhibited highly selective production of formic acid from CO_2. The 'T' component (magnesium tetra-phenyl-porphyrin) of the PGT nanocomposite photocatalyst serves as the light-harvesting complex (electron donor), capturing incoming photons from the visible light. Upon absorbance of photon energy, electronic transitions from the highest occupied molecular orbital (HOMO) to the lowest unoccupied molecular orbital (LUMO) occur, and the electrons are conducted across the 'G' component (aloe-vera-derived graphene), which acts as a multi-electron acceptor. There exists an electron transport chain in the photocatalytic system, which is shown in Fig. 3d. Concurrently, with the assistance of the Rh-complex,[60] the electrons are mediated to the NAD^+, which is then reduced to 1,4-NADH. In this process, the reduced Rh-complex eliminates a proton from the aqueous solution and transfers a hydride ion to NAD^+ and converts it into 1,4-NADH, thereby completing a photocatalytic cycle. This 1,4-NADH cofactor is then consumed by the formate dehydrogenase (FDH) enzyme, which further enables the conversion of CO_2 to HCOOH. The bio-photocatalytic cycle is well-coupled, triggering formic acid production.

2.2. Characterization of the PGT nanocomposite flexible film as an artificial leaf photocatalyst

UV absorption investigations for T, G, and 1% PGT were carried out in solid media. Strong band absorption at 400–600 nm was observed in 1% PGT (Fig. 1a), which is in accordance with that of T. There have already been reports of this type of observation.[61,62] At approximately 420 nm, the absorption coefficients of T and G are low, whereas the absorption of 1% PGT is higher within the same range.

Additionally, the increasing absorbance of 1% PGT in the range of 400 nm to 700 nm shows the enhancement of π–π

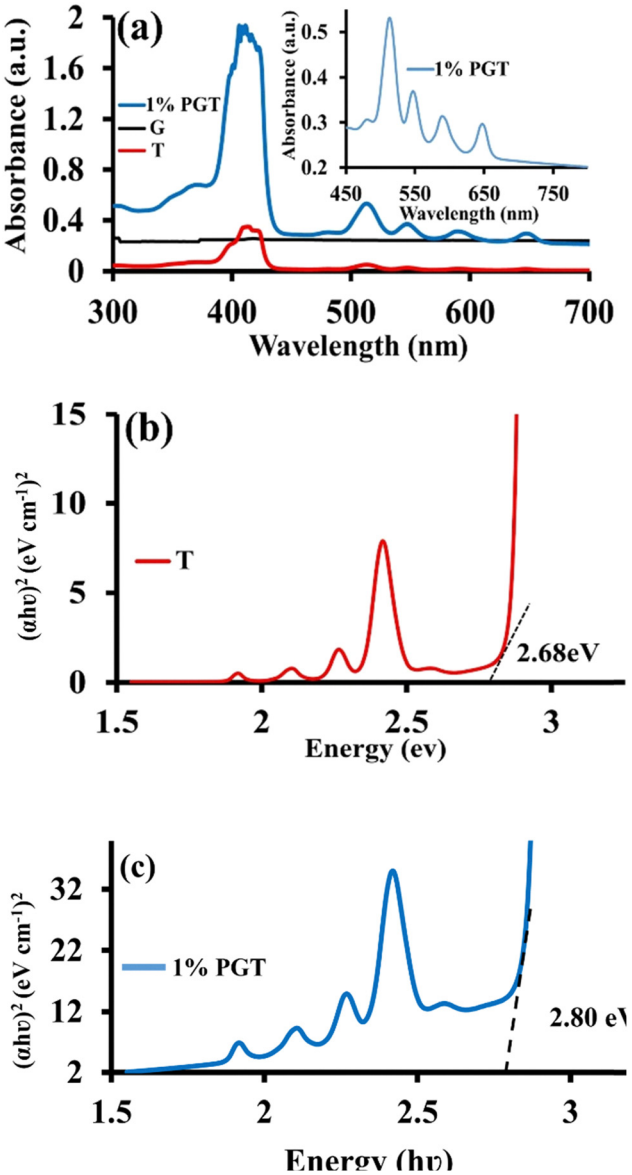

Fig. 1 (a) Diffuse reflectance spectra of the G, T, and 1% PGT photocatalysts. (b) Optical band gap calculation of T, and (c) 1% PGT light-harvesting materials by the Kubelka–Munk (K–M) method.

interactions, high molar extinction coefficient, and efficacious migration of energy and photo-induced electrons among T, G, and P. As shown in Fig. 1b, the band gap of T and 1% PGT are 2.68 and 2.8 eV, respectively, which was calculated by the Kubelka–Munk (K–M) method. This shows that the electronic characteristics of G and P have relaxed in the ground-state attachment of the T core, demonstrating the high efficacy of 1% PGT as a photocatalytic agent for the regeneration of 1,4-NADH, which is crucial in the enzymatic formation of solar fuels/chemicals from CO_2 under sunlight.

Fourier transform infrared (FT-IR) spectroscopy was performed to examine the presence of interfacial bonds between the moieties in the composite.[63] The spectra shown in Fig. 2a explain the modes of the different vibrational frequencies that

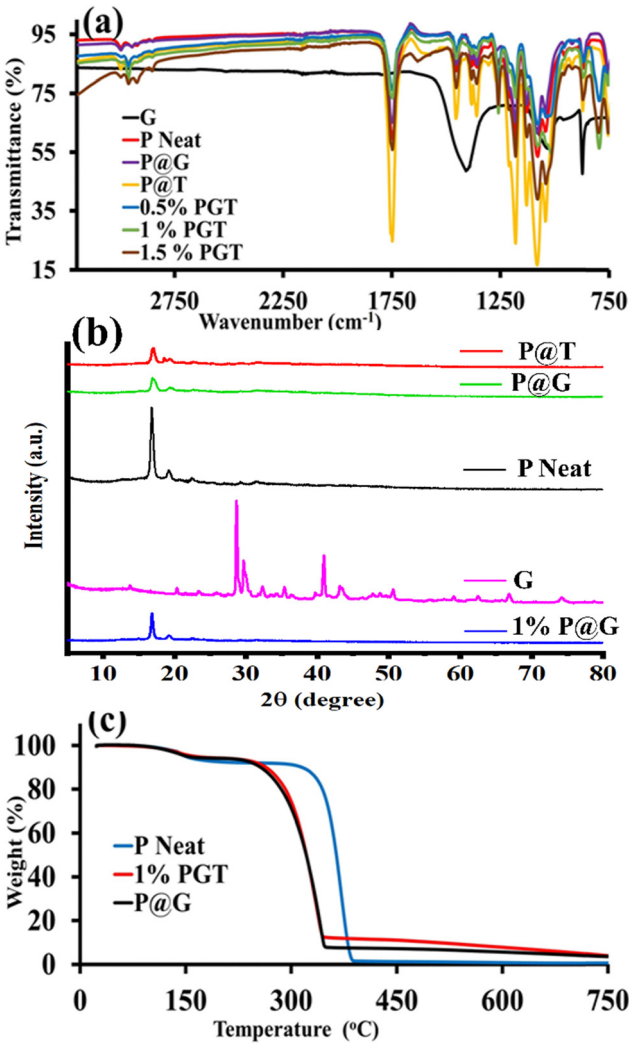

Fig. 2 (a) FTIR spectra of aloe-vera-derived G, P neat, P@G, P@T, 0.5, 1, 1.5% PGT (b) X-ray diffraction of G, P neat, P@G, P@T, and 1% PGT nanocomposite flexible artificial leaf photocatalyst, and (c) TGA plot comparing the mass loss of P neat, P@G, and 1% PGT nanocomposite photocatalyst.

arise due to molecular interaction. The region of interest for G′ is 1720–1020 cm^{-1}, *i.e.*, which shows characteristic peaks for C═O, C–O, and O–H vibrational stretching at 1721 cm^{-1}, 1017 cm^{-1}, and 1418 cm^{-1}, respectively, whereas for neat P, a characteristic peak appears at 1187 cm^{-1} for C–O stretching.[64–66] However, the incorporation of 'P' into G' resulted in different vibrational and stretching peaks at 546 cm^{-1}, 590 cm^{-1}, 740 cm^{-1}, and 843 cm^{-1} in the given spectra in Fig. 2a, which confirms incorporation. Additionally, two distinct infrared peaks were observed for C–C–C bending and CH_2 vibration at 1070 cm^{-1} and 1402 cm^{-1}, respectively.

Nonetheless, if 'T' was incorporated in 'P' instead of 'G', then due to the presence of a pyrrole unit, two characteristic peaks would be observed for C═C and C═N vibrational modes, with a strong absorption band at 1081 cm^{-1} and 1746 cm^{-1}, respectively. The N–H stretching vibration and bending vibration were found to be at 2985 cm^{-1} and 958 cm^{-1}, respectively, which disappear with the insertion of a metal, such as magnesium (in the case of metalloporphyrin). Moreover, all of the vibrations and stretching peaks in the comparative profiles of 0.5% PGT, 1% PGT, and 1.5% PGT correspond to a decrease in transmittance intensity. This FTIR assessment confirms that G and T react with P and produce a new PGT nanocomposite flexible artificial leaf photocatalyst, which improves the cohesion strength and adhesion strength with P. The above study also revealed that reinforcement of G and T in the P composites improves the tensile, flexural, and impact strengths, as well as the hardness of the PGT nanocomposite flexible artificial leaf photocatalyst.[67]

X-ray diffraction (XRD) analysis was performed on a developed sample, including G, P neat, P@G, P@T, and a 1% PGT nanocomposite flexible film as an artificial leaf photocatalyst. In Fig. 2b, there are multiple peaks for G, which is consistent with previous research and shows that graphene typically has a weak, broad peak at 26.12°.[68] The P@G sample exhibited two broader peaks at 16.98° and 19.32°, indicating the presence of P and G. There were broad peaks for P neat and the P@T material, as per a previously reported method.[69] The 1% PGT nanocomposite flexible artificial leaf photocatalyst, noted for its exceptionally high strength, showed additional peaks at 16.84°, 20.01°, and 22.54°, which confirmed the presence of G and T in this newly developed nanocomposite photocatalyst. As a result, the 1% PGT nanocomposite flexible artificial leaf photocatalyst outperformed the other samples, indicating its potential for a variety of applications.

Thermogravimetric analysis (TGA) aids in a better understanding of thermal properties of the composite.[70] Therefore, the thermal degradation and thermal stability were investigated for P neat, P@G, and 1% PGT nanocomposite flexible films as artificial leaf photocatalysts. The weight loss *vs.* temperature curve that was acquired from TGA was used to analyze the thermal stability of the 1% PGT filament. Fig. 2c illustrates how weight loss in the composite sample begins at temperatures over 180 °C, which is when thermal degradation began. Between 110 °C and 300 °C, the P and PGT composites lost approximately 1% and 4% of their weight, respectively.

There was a weight loss of nearly 95% for the composite sample (compared to a 100% loss for pure P) when the samples were heated from room temperature to 750 °C in an N_2 environment, confirming G and T materials. From the TGA plot of the residue, it is obvious that G and T are the principal filler components included in the nanocomposite photocatalyst. For the P and PGT nanocomposite flexible films as artificial leaf photocatalysts, weight loss was approximately 100% and 95% between 400 °C and 350 °C, respectively. This suggests that the PGT nanocomposite homogeneity caused the composite to gradually degrade under control.[71,72]

2.3. Electrochemical band gap analysis and fabrication of PGT nanocomposite flexible film for artificial leaf photocatalysis

The redox potential of T and the 1% PGT nanocomposite flexible artificial leaf photocatalyst was examined by cyclic voltammetry (CV) with a glassy carbon electrode (working

electrode), calomel electrode (reference electrode), and platinum electrode (counter electrode) in 0.1 M tetrabutylammonium hexafluorophosphate (TBAHFP) electrolyte.[73] The CV experiment was performed to demonstrate the oxidation and reduction potential of T and the 1% PGT nanocomposite flexible artificial leaf photocatalyst. In Fig. 3a, the oxidation potential was observed at an anodic peak of T (+1.29 V) and a cathodic peak (−1.24 V). The oxidation and reduction potential of 1% PGT was observed at an anodic peak (+1.22 V) and cathodic peak (−1.20 V). The 1% PGT showed an anodic shift of oxidation potential, which designates the effective migration of charge carriers from the 1% PGT to the Rh-complex.

The photoelectrical property of 1% PGT originates from the excitation of electrons from the HOMO (5.72 eV) to the LUMO (3.30 eV), followed by the transfer of the excited electrons into the Rh-complex (Fig. 3d).[64,74] The vicinity and potential gradient between the light-harvesting and the Rh center enable effective electron transfer from the 1% PGT photocatalyst to the Rh. Furthermore, upon comparing the band gaps of T (2.59 eV) and 1% PGT (2.42 eV), there is a narrower band gap for the 1% PGT photocatalyst, which allows electrons from the excited 1% PGT to easily move to the Rh-complex. This finding is consistent with band gap predictions using the Tauc Method, demonstrating the effective electron transport mechanism from 1% PGT to the Rh-complex in this photocatalytic system. The Tafel plot elucidates the photocatalytic activity of T and the 1% PGT nanocomposite flexible artificial leaf photocatalyst.

The Tafel slope on a Tafel plot is inversely associated with the photocatalytic activity of a material. A high slope denotes a rapid reaction rate, whereas a shallow slope indicates a slower rate. In photocatalysis, a steep slope indicates effective electron–hole pair formation and separation, which leads to high photocatalytic activity. Fig. 3b shows the Tafel plot of T and the 1% PGT photocatalyst. The Tafel slope of 1% PGT is lower than that of T, indicating the better photocatalytic activity of our newly designed 1% PGT.

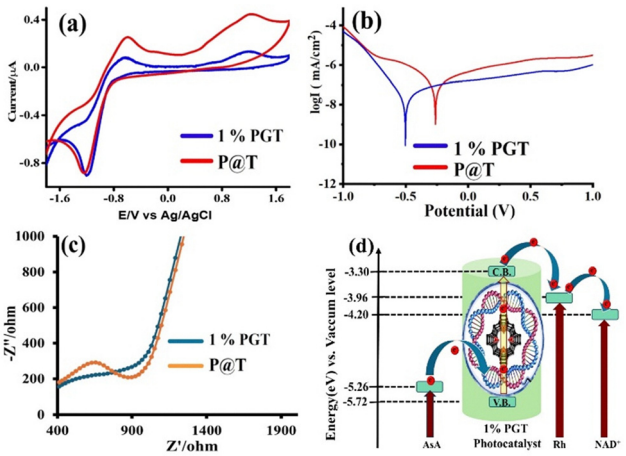

Fig. 3 (a) Cyclic voltammetry curve for 1% PGT and P@T, (b) Tafel plot for 1% PGT and P@T, (c) EIS for the 1% PGT and P@T photocatalysts, and (d) energy level diagram for the 1% PGT photocatalyst.

Electrochemical impedance spectroscopy (EIS) is an effective method for studying charge carrier dynamics in a three-electrode system. Our study included EIS analysis at frequencies ranging from 100 kHz to 0.1 Hz. The AC amplitude was tuned to 5 mV to study charge transfer and transport in the system. To ensure a uniform testing environment, we maintained a working/reference electrode separation of 1 cm during the electrochemical studies.[73] Fig. 3c shows Nyquist plots of P@G and the 1% PGT photocatalyst. The Nyquist plot consists of a plot of the imaginary part ($-Z'$) *versus* the real part (Z') of the impedance. The plot frequently takes the shape of a semicircle, and the arc radius of this semicircle is proportional to the charge transfer resistance of the system. The smaller the semicircle arc radius, the lower the charge transfer resistance, which leads to high charge transfer. Fig. 3c shows a small arc radius for 1% PGT as compared to P@G. This evidence shows that the charge carrier dynamics of the newly synthesized 1% PGT photocatalyst are more optimal due to a lower charge transfer resistance as compared to P@G.

A plausible mechanism of transference for photogenerated charge within the 1% PGT photocatalyst is demonstrated in Fig. 3d. Upon visible light irradiation, the electrons from the valence band (−5.72 eV) of the 1% PGT photocatalyst jump to the conduction band (−3.30 eV), generating electron–hole pairs. Ascorbic acid (AsA) acts as a sacrificial agent that quenches the valence band of the 1% PGT photocatalyst. The electrons from the conduction band are then transferred to NAD^+ (−4.2 eV) with the assistance of the Rh-complex electron mediator (−3.96 eV). This movement of electrons from the photocatalyst to the NAD^+ leads to the formation of 1,4-NADH cofactor.[75]

2.4. Exploring the morphology of the photocatalysts

Field emission scanning electron microscopy (FE-SEM) is a morphological research tool for capturing microstructure images of developed materials. Fig. 4a–d shows FE-SEM images of P neat, P@G, P@T, and the 1% PGT nanocomposite flexible artificial leaf photocatalyst. Fig. 4a shows the structure of P neat,[76] while the yellow circle in (b) indicates the presence of the G content in the P matrix.[77] Fig. 4c shows the presence of the T content in the P matrix in the form of a crumbling structure.[64] Fig. 4d shows the presence of G and T particles in the matrix. The G and T particles have joints and protuberances that are attached to the surface of P, and these participate in mechanical interlocking and reduce fatigue crack propagation in the composite. Overall, the PGT nanocomposite photocatalyst exhibits good dispersion.

2.5. Mechanical studies of the designed PGT nanocomposite flexible film as an artificial leaf photocatalyst

2.5.1. Study of the tensile strength of the designed materials. The mechanical properties of the newly developed nanocomposite photocatalyst were determined using tensile tests. These tests entail the application of force to a material until it reaches its breaking point, thereby enabling the determination of its tensile strength and elongation properties (Fig. S1, ESI†).

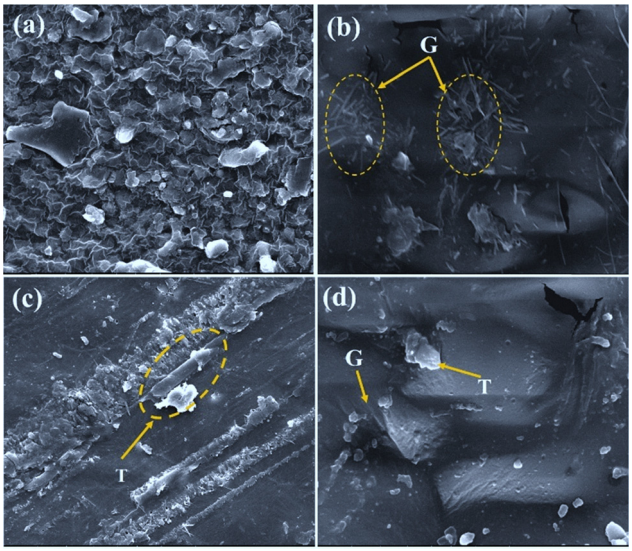

Fig. 4 SEM analysis of (a) P neat, (b) P@G, (c) P@T, and (d) the 1% PGT nanocomposite flexible artificial leaf photocatalyst.

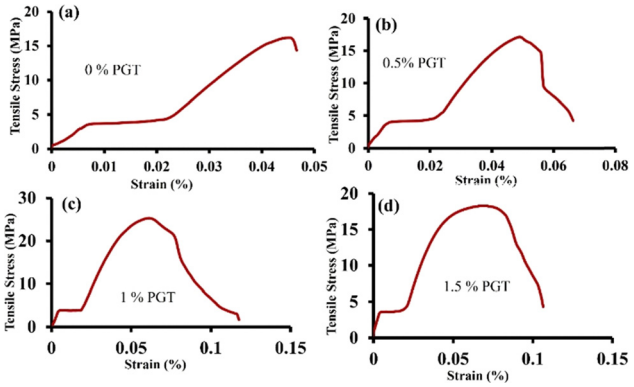

Fig. 5 Stress *vs.* strain curve from the tensile test for the nanocomposite flexible artificial leaf photocatalysts: (a) 0% PGT, (b) 0.5% PGT, (c) 1% PGT, (d) 1.5% PGT nanocomposite flexible films as artificial leaf photocatalysts.

The specimens, with dimensions of 63.5 mm × 19 mm × 3 mm, were tested using a universal testing machine (UTM Model-EZ50) with a maximum capacity of 50 KN at room temperature, following the guidelines set by ASTM D638 standards.

Tensile tests were conducted on nanocomposite photocatalyst specimens with varying concentrations of PGT (0%, 0.5%, 1%, and 1.5%), as depicted in Fig. S2 (ESI†). For each variation, three specimens were tested, and the average outcomes are presented in Table 1. Fig. S2(a and b) (ESI†) shows the specimens before and after testing, demonstrating the successful tensile tests. Moreover, Fig. 5 illustrates the stress–strain characteristics of the tensile samples, offering insights into their mechanical efficacy. The experimental data demonstrate that incorporating G reinforcement consistently enhances the tensile strength by up to 1%. This enhancement is due to G and T developing strong cross-links with the matrix, delaying crack initiation and propagation.[78,79] However, after a certain amount of increased fractions of G, the load-carrying capacity decreases due to G agglomeration.

This phenomenon emphasizes the critical importance of optimizing the G content in the nanocomposite to achieve optimal mechanical properties. Thus, the optimum value for maximum tensile strength was obtained for the 1% PGT nanocomposite flexible artificial leaf photocatalyst, and the value of the maximum load capacity is 589.49 N. This highly tensile nanocomposite photocatalyst can be applied to scaffolding applications in human tissue engineering.

2.5.2. Flexural test. A flexural test, also known as a bending test, is a material testing method used to determine the behaviour of a material when subjected to bending loads.[80] This test is particularly important in assessing the strength and stiffness of materials, especially those used in structural applications such as construction materials, metals, plastics, and composites.[81] As shown in Fig. S3 (ESI†), the flexural test was performed as per ASTM standard D790 (125 × 12.7 × 3.2) on the newly developed PGT nanocomposite flexible artificial leaf photocatalysts.[82] For each composition, three specimens were examined under a three-point bending mode. Fig. 6 shows the stress–strain behaviour of 0%, 0.5%, 1%, and 1.5% PGT nanocomposite flexible artificial leaf photocatalysts. The calculated flexural strength and load are detailed in Table 2, which shows that reinforcement of G and T in the P composites increased the flexural strength. Notably, the highest flexural strength was found for the 1% PGT nanocomposite flexible film as an artificial leaf photocatalyst. However, the use of nanomaterials promotes agglomeration, which serves as a site for crack propagation.[83–85]

2.5.3. Impact testing. The impact test evaluates the materials' energy absorption and impact resistance of the nanocomposite specimens during the collision phase.[86] The impact test used an interchangeable pendulum-type hammer Izod impact tester machine with a pendulum speed of 346 m s^{-1}. A pivoting arm is raised to a specific height and then released. As shown in Fig. 7a, the striker swings down, hitting a notched sample, and subsequently breaks the specimen. The Izod impact test

Table 1 Mechanical properties of the developed nanocomposite flexible artificial leaf photocatalyst

S. no.	Developed specimen code	Composition of the developed specimen	Tensile properties		
			Tensile strength (MPa)	Tensile load (N)	Strain (%)
1	0% PGT	P, 0% G, T	16.184	307.30	4.761
2	0.5% PGT	P, 0.5% G, T	17.125	432.58	6.771
3	1.0% PGT	P, 1% G, T	25.322	589.49	11.755
4	1.5% PGT	P, 1.5% G, T	18.292	349.56	10.878

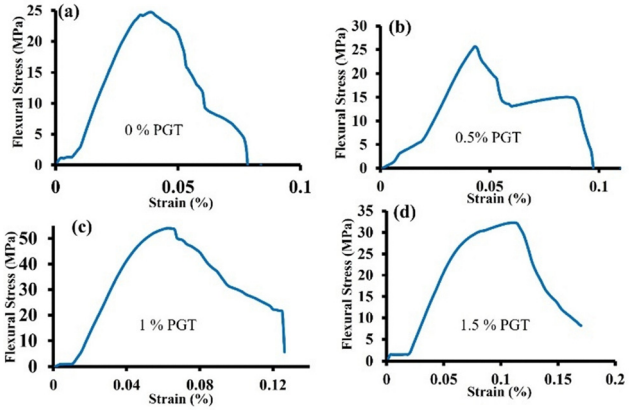

Fig. 6 Flexural stress *vs.* strain curve of the flexural test for nanocomposite flexible artificial leaf photocatalysts (a) 0% PGT, (b) 0.5% PGT, (c) 1% PGT, and (d) 1.5% PGT.

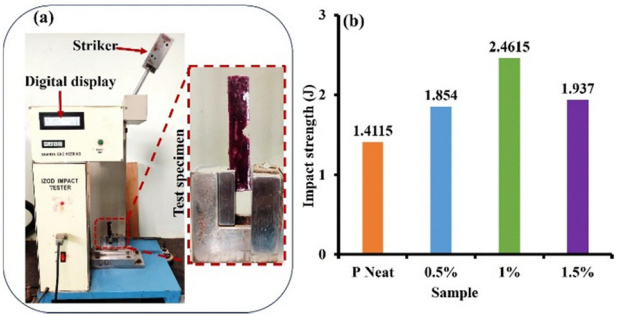

Fig. 7 (a) Impact test setup and (b) impact strength of a tested specimen with varying wt% of G.

was performed according to the ASTM D256 standard with a 64 × 12.7 × 3 mm specimen size.[87]

The role of the G and T content on the impact behaviour of the developed nanocomposite photocatalysts is shown in Fig. 7b. The results demonstrated that the impact strength of the P neat composite absorbed energy up to 1.4115 J. In contrast, reinforcement of G and T in the P neat composite increased the energy absorption capacity. The maximum impact strength of 2.461 J was obtained for the 1% PGT nanocomposite flexible artificial leaf photocatalyst. The impact strengths for the 0.5% and 1.5% PGT nanocomposite photocatalysts are shown at 1.854 J and 1.937 J, respectively. The developed nanocomposite with 0.5% and 1.5% PGT reinforcement shows a slightly increased enhancement as compared to the P neat composite. An overall 23%, 42.65%, and 27.129% improvement was observed in impact strength for the 0.5%, 1%, and 1.5% PGT nanocomposite flexible artificial leaf photocatalysts, respectively, as compared to the P neat composite.

A decreasing trend in impact strength was obtained after increasing fractions of the reinforcement of G in the P composite were tested. This may be due to the agglomeration effect in the matrix resin, which promotes pre-cracking in the polymer.[88] During this experiment, the matrix initially absorbed the impact load. The strength of the matrix was enhanced through modifications of its G and T content. Incorporating additional G up to 1.5% fractions did not noticeably change the results, indicating that the matrix plays a prominent role in the composite's capacity to absorb impact energy.[89] In this impact strength study, G and T play a vital role in enhancing the impact strength and increasing the energy-absorbing capacity.

2.5.4. Shore D hardness. A Shore D durometer tester determined the surface hardness of the newly developed nanocomposite photocatalyst. Shore D hardness measures a composite's resistance to needle penetration at a given spring force.[72,90] The hardness is graded on a scale of 0 to 100 and classified as A or D. In this test, a higher numerical value indicates greater hardness, with A denoting flexibility and D indicating rigidity. The shore D hardness test involved the testing of three specimens for each developed nanocomposite (P neat, 0.5%, 1%, and 1.5% PGT nanocomposite flexible artificial leaf photocatalysts) and calculating the average value. According to the literature review, the hardness test results influence mechanical properties such as shear strength, flexural strength, tensile strength, modulus of elasticity, and impact strength.

Fig. 8 depicts the effect of reinforcement of the P and T content on the hardness of the nanocomposite photocatalyst. The hardness value of the PGT nanocomposite flexible artificial leaf photocatalyst increased from 54.52 J (P neat) to 60.4, 65.08, and 63.96 with reinforcement of 0.5%, 1%, and 1.5 wt% PGT, respectively. The optimal results obtained with the 1 wt% PGT nanocomposite photocatalyst were due to well-developed interfacial interaction and enriched G dispersion. Compared to the P neat composite, the hardness increased by 10.78%, 19.36%, and 17.31% at 0.5, 1, and 1.5 wt% PGT in the nanocomposite flexible artificial leaf photocatalyst, respectively. The results of this investigation indicate that the reinforcement of G and T in P improves mechanical properties.

2.6. Green alchemy: harnessing light for 1,4-NADH regeneration and formic acid synthesis from CO_2

A series of Photocatalytic experiments was performed to study the photocatalytic activities of P, T, 0.5% PGT, 1% PGT, and

Table 2 Flexural test results for the developed nanocomposite photocatalysts

S. no.	Developed specimen code	Composition of the developed specimen	Flexural properties		
			Maximum bending stress (MPa)	Maximum bending strain (%)	Tensile load (N)
1	0% PGT	P, 0% G, T	30.019	6.2054	85.835
2	0.5% PGT	P, 0.5% G, T	31.196	15.787	106.91
3	1% PGT	P, 1% G, T	32.244	17.18	163.01
4	1.5% PGT	P, 1.5% G, T	31.577	17.513	138.23

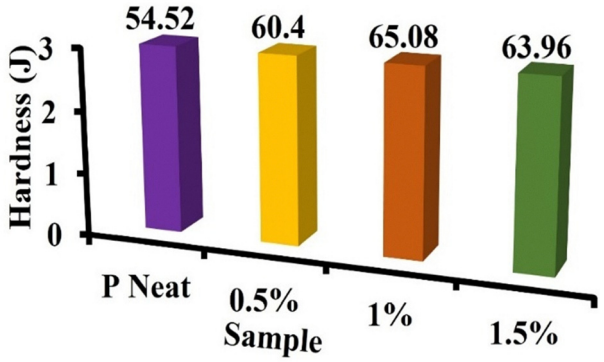

Fig. 8 The hardness of P neat, and the 0.5, 1, and 1.5 wt% PGT nanocomposite photocatalysts.

1.5% PGT for the visible light-driven photoregeneration of 1,4-NADH. The concentration of photogenerated 1,4-NADH was measured by a spectrophotometer.[91] As shown in Fig. 9, the 1% PGT nanocomposite flexible film as an artificial leaf is significantly effective for 1,4-NADH photoregeneration, constantly accumulating up to 61.09% with time linearity. However, the P, T, 0.5% PGT, and 1.5% PGT photocatalysts provided only a 0.00%, 9.27%, 30.54%, and 60.91% yield of regenerated 1,4-NADH, respectively (Fig. 9a).

Additional experiments were performed to study the photocatalytic performance of P, T, 0.5% PGT, 1% PGT, and 1.5% PGT for the visible-light-driven artificial photosynthesis of formic acid from CO_2. The amount of formic acid was measured by UV-visible spectroscopy and high-performance liquid chromatography (HPLC, Model LC-20AP). As shown in Fig. 9b, the formic acid yield linearly increased with the reaction time when a 1% PGT nanocomposite flexible film, as an artificial leaf, was used as a photocatalyst. The efficiency of the 1% PGT nanocomposite flexible film as an artificial leaf for the production of formic acid for 2 h was 146.62 μmol, while those for P, T, 0.5% PGT, and 1.5% PGT were 0.00, 22.24, 73.31, and 122.18 μmol, respectively. These investigations demonstrate

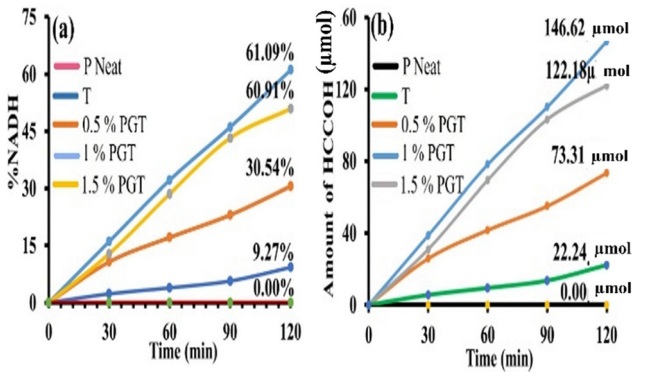

Fig. 9 The photocatalytic activity of P, T, 0.5% PGT, 1% PGT, and 1.5% PGT in the solar light-driven artificial photosynthesis of formic acid from CO_2 and 1,4-NADH photoregeneration. (a) Photoregeneration of 1,4-NADH, and (b) the artificial photosynthesis of formic acid from CO_2 driven by solar light.

that the 1% PGT nanocomposite flexible film functions as a superior artificial leaf photocatalyst compared to the other tested photocatalysts, owing to its excellent mechanical properties.

The incident light is absorbed at T, where photoexcitation occurs, and the generated electrons move into P *via* stable mechanical bonding, such as that which occurs with optimal bending strength, tensile strength, and shear strength. The energy level alignment between the LUMO of T and the conduction band edges of P@G was used to assess the electron-transfer efficiency.

Ascorbic acid (AsA) was used as a hole scavenger to prevent electron transport from P@G to the photoexcited T. Therefore, rather than the other way around, it is simple to move the photoexcited electrons produced in T into P@G. The possibility of electrons being transported into the Rh-complex is increased by the highly surface-active sites and exceptionally high carrier mobility of P@G,[92] thereby accelerating the chemical processes leading to the formation of 1,4-NADH. In addition, P@G transports multiple electrons by serving as an electron reservoir. Due to strong Coulombic repulsion between localised electrons, electron addition in most molecular systems has a very high energy cost. In P@G, because of the delocalized nature of wave functions throughout the entire P@G surface (extending many μm), multi-electron addition or removal is conceivable.

4. Experimental

4.1. Materials

Nicotinamide adenine dinucleotide (β-NAD^+), formate dehydrogenase, 2,2′-bipyridine, (pentethylcyclopentadienyl) rhodium(III) chloride dimer, *N*,*N*-dimethylformamide, polylactic acid, chloroform, cyclohexane, silica gel, magnesium chloride ($MgCl_2$), iodine, pyrrole, dichloromethane, *p*-chloranil, benzaldehyde, ascorbic acid, and monobasic and dibasic phosphate buffers were purchased from TCI.

4.2. Lighting the path to renewable energy: harnessing photocatalysis for 1,4-NADH production

Using sunlight and an inert atmosphere, photochemical regeneration of 1,4-NADH was carried out at ambient temperature in a quartz reactor. The photocatalytic regeneration of 1,4-NADH was performed in 3.1 mL of sodium phosphate buffer (100 mM, pH 7.0) that contained the following reaction components: β-NAD^+ (1.24 mmol), rhodium (Rh)-complex (0.62 mmol), synthesised as per a previous study,[60] AsA (1.24 mmol), and film photocatalyst (1 × 1 cm^2). A UV-vis spectrophotometer was used to track the regeneration of 1,4-NADH. In the ^{1}H-NMR spectra of 1,4-NADH, a peak for 1,4-NADH at 6.55 ppm arises due to hydrogen atoms on the pyridine ring (a solvation effect), as shown in Fig. S4 (ESI†).[93]

4.3. Transforming CO_2 into formic acid fuel

The production of formic acid from CO_2 was also carried out in a quartz reactor at ambient temperature in an inert environment using sunlight. The procedure used a film photocatalyst (1 × 1 cm^2), β-NAD^+ (1.24 mmol), Rh-complex (0.62 mmol),

and formate dehydrogenase (3 units) in 3.1 mL of sodium phosphate buffer (100 mM, pH 7.0) with AsA (1.24 mmol) in the presence of CO_2. After bubbling CO_2 for 1 h in the absence of light (light off), the reactor was exposed to visible light (light on). The quantity of formic acid was determined using UV-visible spectroscopy and HPLC.

4.4. Synthesis of aloe-vera-derived graphene (G)

As shown in Scheme 2, raw aloe vera was cut into small pieces and washed with deionized (DI) water several times after the green skin was carefully removed. The internal part of the aloe vera leaf was ground in a mixer along with ethanol. After that, the prepared mixture was stirred at 550 rpm at 150 °C. The stirring process continued until the mixed solution became dry. After drying, a specific amount of the dried aloe vera was transferred to a crucible and heated in a muffle furnace at 500 °C for 4 h. After the heating process, the crucible was removed from the muffle furnace and allowed to cool at room temperature, which yielded aloe-vera-derived graphene.[64]

4.5. Synthesis of light-harvesting magnesium tetra-phenyl-porphyrin (T)

A previously reported procedure[94] was followed for the synthesis of tetra-phenyl-porphyrin (TPP). Benzaldehyde (1 mmol), iodine (0.21 eq.), and pyrrole (1 mmol) were added to 10 mL of dichloromethane (DCM). Following the initial activation (300 W, 35 °C), TLC revealed that the benzaldehyde was completely converted. After adding *para*-chloranil (0.75 eq.), a second activation (300 W, 35 °C) was carried out. Using DCM/petroleum ether (1 : 1) as the eluent, the mixture was purified by flash chromatography. A purple solid (59 mg, 36%) (tetra-phenyl-porphyrin) was obtained. Finally, the solution containing 0.25 g of tetra-phenyl-porphyrin and 0.28 g of $MgCl_2$ in 10 mL of DMF was refluxed for approximately 1 h. After refluxing, the solution was cooled. After that, 200 mL of distilled water was added to the cooled solution, and it was maintained in an ice bath for 15 min. Following filtering, a final solid precipitate of Mg-TPP was obtained. The product was rinsed with distilled water and left to dry (Scheme 3).[94,95]

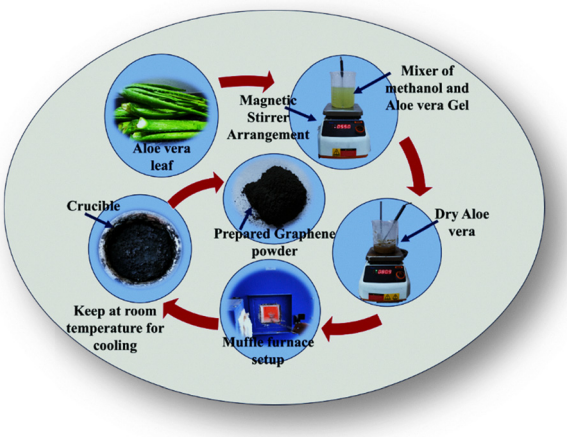

Scheme 2 Synthesis of aloe-vera-derived graphene (G) from green aloe vera leaf.

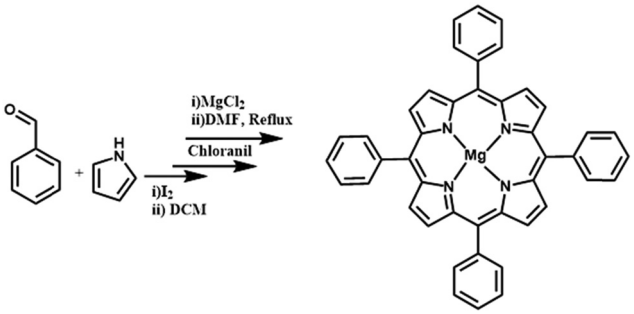

Scheme 3 Synthesis of magnesium tetra-phenyl-porphyrin (Mg-TPP ~ T) *via* the condensation method.

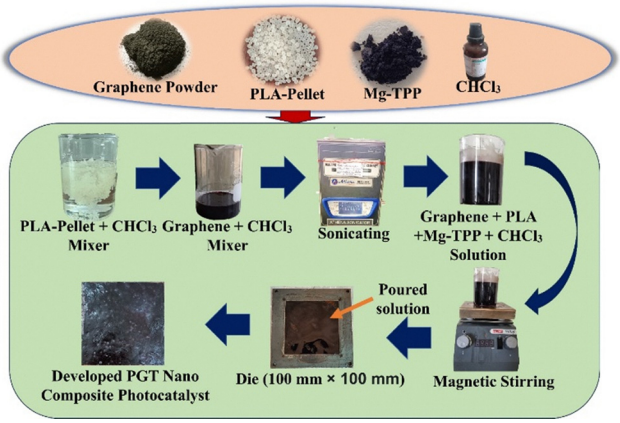

Scheme 4 Synthesis of the PGT nanocomposite flexible artificial leaf photocatalyst.

4.6. Development of the aloe-vera-derived PGT nanocomposite flexible artificial leaf photocatalyst

Scheme 4 depicts the fabrication of a PGT nanocomposite flexible artificial leaf photocatalyst. During the fabrication processes to prevent agglomeration, G powder was initially dispersed in chloroform ($CHCl_3$), and then sonicated at 45 kHz for an hour. P pellets were then added to the mixture, along with $CHCl_3$, and the synthesized G powder was stirred at 170 °C for 2 h and 30 min. The resin blend was poured into a 100 × 100 × 3 mm mold and dried for under the sun for 24 h. The fabricated composite was cut for mechanical strength testing under ASTM standards, followed by tensile, flexural, impact, and hardness tests, as well as 1,4-NADH regeneration. For comparative mechanical strength testing, four types of specimens were developed: P neat, 0.5%, 1%, and 1.5% PGT nanocomposite flexible artificial leaf photocatalysts.

5. Conclusions

The fabrication of an artificial leaf composed of a 1% PGT donor–acceptor nanocomposite represents a remarkable

milestone in multifunctional material design. This flexible film photocatalyst harnesses solar energy with exceptional efficiency, enabling the regeneration of 1,4-NADH and the subsequent enzymatic reduction of CO_2 to formic acid *via* formate dehydrogenase. This system achieves a regeneration efficiency of 61.09 ± 0.59% and a formic acid yield of 146.62 ± 1.μ6 μmol, clearly demonstrating its potential as a solar-driven platform for carbon capture and conversion into value-added chemicals. Beyond its photocatalytic proficiency, the 1% PGT nanocomposite exhibits excellent mechanical robustness, including a strain capacity of 11.755%, bending strength of 32.244 MPa, tensile strength of 25.322 MPa, maximum tensile load of 589.49 N, and impact resistance of 2.4615 J. These mechanical characteristics indicate that the material is highly suitable for biomedical applications such as scaffold-based tissue engineering, where flexibility, biocompatibility, and structural integrity are essential.

Comparative analysis underscores the superior performance of the 1% PGT nanocomposite over its 0.5% and 1.5% counterparts. This indicates an optimal balance between mechanical strength and photocatalytic activity at this composition, highlighting the critical importance of precise material tuning. Such optimization is vital for enhancing the functional performance in targeted applications. Altogether, the 1% PGT nanocomposite stands out as a versatile and high-performance material, merging environmental and biomedical functionalities. Its dual role as an efficient artificial leaf for CO_2 fixation and as a mechanically robust scaffold for tissue regeneration highlights its transformative potential in sustainable energy conversion and regenerative medicine. This work not only advances photocatalytic materials but also offers a blueprint for designing next-generation multifunctional nanocomposites capable of addressing urgent global and environmental challenges.

Author contributions

These authors contributed equally to this work.

Conflicts of interest

The authors declare no competing financial interests.

Data availability

All data underlying the results are available as part of the article, and no additional source data are required.

Acknowledgements

This presented work is financially supported by the Uttar Pradesh Council of Science and Technology, Lucknow, India, under research project scheme UPCST R&D project ID-1541. The authors are thankful to MMMUT, Gorakhpur-273010, U. P., India for providing the platform for research and Dr. Baeg for main research project KRICT. The authors would also like to acknowledge the kind support of the Council of Science and Technology, Lucknow, under the Govt. of Uttar Pradesh, India.

References

1 G. Wang, L. Zhang and J. Zhang, *Chem. Soc. Rev.*, 2012, **41**, 797.
2 P. A. T. Kelly, C. J. Davis and G. M. Goodwin, *Neuroscience*, 1988, **25**, 907.
3 S. S. Balaji and M. Sathish, *RSC Adv.*, 2014, **4**, 52256.
4 B. Amutha and M. Sathish, *J. Solid State Electrochem.*, 2015, **19**, 2311.
5 K. Subramani, D. Jeyakumar and M. Sathish, *Phys. Chem. Chem. Phys.*, 2014, **16**, 4952.
6 K. Subramani, N. Lakshminarasimhan, P. Kamaraj and M. Sathish, *RSC Adv.*, 2016, **6**, 15941.
7 E. Frackowiak, *Phys. Chem. Chem. Phys.*, 2007, **9**, 1774.
8 R. J. Mo, Y. Zhao, M. Wu, H. M. Xiao, S. Kuga, Y. Huang, J. P. Li and S. Y. Fu, *RSC Adv.*, 2016, **6**, 59333–59342.
9 F.-C. Wu, R.-L. Tseng, C.-C. Hu and C.-C. Wang, *J. Power Sources*, 2004, **138**, 351.
10 F.-C. Wu, R.-L. Tseng, C.-C. Hu and C.-C. Wang, *J. Power Sources*, 2005, **144**, 302.
11 P. Sharma and T. S. Bhatti, *Energy Convers. Manage.*, 2010, **51**, 2901.
12 B. E. Conway, V. Birss and J. Wojtowicz, *J. Power Sources*, 1997, **66**, 1.
13 L. L. Zhang and X. S. Zhao, *Chem. Soc. Rev.*, 2009, **38**, 2520.
14 D. Puthusseri, V. Aravindan, S. Madhavi and S. Ogale, *Energy Environ. Sci.*, 2014, **7**, 728.
15 S. Bai, G. Tan, X. Li, Q. Zhao, Y. Meng, Y. Wang, Y. Zhang and D. Xiao, *Chem. – Asian J.*, 2016, **11**, 1828.
16 Y.-Y. Wang, B.-H. Hou, H.-Y. Lü, C.-L. Lü and X.-L. Wu, *ChemistrySelect*, 2016, **1**, 1441.
17 T. E. Rufford, D. Hulicova-Jurcakova, K. Khosla, Z. Zhu and G. Q. Lu, *J. Power Sources*, 2010, **195**, 912.
18 M. Wahid, D. Puthusseri, D. Phase and S. Ogale, *Energy Fuels*, 2014, **28**, 4233.
19 T. E. Rufford, D. Hulicova-Jurcakova, Z. Zhu and G. Q. Lu, *Electrochem. Commun.*, 2008, **10**, 1594.
20 M. S. Balathanigaimani, W.-G. Shim, M.-J. Lee, C. Kim, J.-W. Lee and H. Moon, *Electrochem. Commun.*, 2008, **10**, 868.
21 X. Wu, W. Xing, J. Florek, J. Zhou, G. Wang, S. Zhuo, Q. Xue, Z. Yan and F. Kleitz, *J. Mater. Chem. A*, 2014, **2**, 18998.
22 J. Wang and S. Kaskel, *J. Mater. Chem.*, 2012, **22**, 23710.
23 Q. Cao, K.-C. Xie, Y.-K. Lv and W.-R. Bao, *Bioresour. Technol.*, 2006, **97**, 110.
24 J. Sahira, A. Mandira, P. B. Prasad and P. R. Ram, *Res. J. Chem. Sci.*, 2013, **2231**, 606X.
25 M. Sathish, S. Mitani, T. Tomai and I. Honma, *J. Mater. Chem. A*, 2014, **2**, 4731.
26 M. Beidaghi and Y. Gogotsi, *Energy Environ. Sci.*, 2014, **7**, 867.
27 R. Currie, S. Mottaghi-Tabar, Y. Zhuang and D. S. A. Simakov, *Ind. Eng. Chem. Res.*, 2019, **58**, 12964.

28 D. Ferrah, A. R. Haines, R. P. Galhenage, J. P. Bruce, A. D. Babore, A. Hunt, I. Waluyo and J. C. Hemminger, *ACS Catal.*, 2019, **9**, 6783.
29 G. Takalkar, R. R. Bhosale, F. AlMomani and M. Khraisheh, *Fuel*, 2019, **257**, 115965.
30 Y. Song, X. Zhang, K. Xie, G. Wang and X. Bao, *Adv. Mater.*, 2019, **31**, 1902033.
31 B. M. Tackett, E. Gomez and J. G. Chen, *Nat. Catal.*, 2019, **2**, 381.
32 A. Lisovskaya and D. M. Bartels, *Radiat. Phys. Chem.*, 2019, **158**, 61.
33 D. C. Grills, J. A. Farrington, B. H. Layne, S. V. Lymar, B. A. Mello, J. M. Preses and J. F. Wishart, *J. Am. Chem. Soc.*, 2014, **136**, 5563.
34 J. Grodkowski and P. Neta, *J. Phys. Chem. B*, 2001, **105**, 4967.
35 X. Liu, F. Kang, C. Hu, L. Wang, Z. Xu, D. Zheng, W. Gong, Y. Lu, Y. Ma and J. Wang, *Nat. Chem.*, 2018, **10**, 1201.
36 A. Efrati, C.-H. Lu, D. Michaeli, R. Nechushtai, S. Alsaoub, W. Schuhmann and I. Willner, *Nat. Energy*, 2016, **1**, 1.
37 P. Wang, S. Wang, H. Wang, Z. Wu and L. Wang, *Part. Part. Syst. Charact.*, 2018, **35**, 1700371.
38 M. J. Kang, C. W. Kim, A. U. Pawar, H. G. Cha, S. Ji, W.-B. Cai and Y. S. Kang, *ACS Energy Lett.*, 2019, **4**, 1549.
39 U. Kang, S. H. Yoon, D. S. Han and H. Park, *ACS Energy Lett.*, 2019, **4**, 2075.
40 C.-H. Huang and C.-S. Tan, *et al.*, *Aerosol Air Qual. Res.*, 2014, **14**, 480.
41 A. Meng, L. Zhang, B. Cheng and J. Yu, *ACS Appl. Mater. Interfaces*, 2018, **11**, 5581.
42 C. Kim, K. M. Cho, A. Al-Saggaf, I. Gereige and H.-T. Jung, *ACS Catal.*, 2018, **8**, 4170.
43 S. Wang, M. Xu, T. Peng, C. Zhang, T. Li, I. Hussain, J. Wang and B. Tan, *Nat. Commun.*, 2019, **10**, 676.
44 Z. Sun, T. Ma, H. Tao, Q. Fan and B. Han, *Chem*, 2017, **3**, 560.
45 N. Zhang, R. Long, C. Gao and Y. Xiong, *Sci. China Mater.*, 2018, **61**, 771.
46 I. Ganesh, *et al.*, *Mater. Sci. Appl.*, 2011, **2**, 1407.
47 L. Wang, W. Chen, D. Zhang, Y. Du, R. Amal, S. Qiao, J. Wu and Z. Yin, *Chem. Soc. Rev.*, 2019, **48**, 5310.
48 S. Xie, Q. Zhang, G. Liu and Y. Wang, *Chem. Commun.*, 2016, **52**, 35.
49 J. Sarkar and S. Bhattacharyya, *Arch. Thermodyn.*, 2012, **33**, 23.
50 S. Singh, R. K. Yadav, T. W. Kim, C. Singh, P. Singh, A. P. Singh, A. K. Singh, A. K. Singh, J. O. Baeg and S. K. Gupta, *React. Chem. Eng.*, 2022, **7**, 1566.
51 H. L. Nguyen and A. Alzamly, *ACS Catal.*, 2021, **11**, 9809.
52 Y. Doi, M. Banba and A. Vertut-Doi, *Biochemistry*, 1991, **30**, 5769.
53 J. Zhao, L. Xue, Z. Niu, L. Huang, Y. Hou, Z. Zhang, R. Yuan, Z. Ding, X. Fu, X. Lu and J. Long, *J. Power Sources*, 2021, **512**, 230532.
54 H. Zhang, P. Zhang, J. Zhao, Y. Liu, Y. Huang, H. Huang, C. Yang, Y. Zhao, K. Wu, X. Fu, S. Jin, Y. Hou, Z. Ding, R. Yuan, M. B. J. Roeffaers, S. Zhong and J. Long, *Angew. Chem., Int. Ed.*, 2021, **60**, 16009.
55 J. Zhao, L. Huang, L. Xue, Z. Niu, Z. Zhang, Z. Ding, R. Yuan, X. Lu and J. Long, *J. Energy Chem.*, 2023, **79**, 601.
56 M. Khalil, J. Gunlazuardi, T. A. Ivandini and A. Umar, *Renewable Sustainable Energy Rev.*, 2019, **113**, 109246.
57 R. J. Detz and B. van der Zwaan, *Energy Policy*, 2019, **133**, 110938.
58 S. Kar, A. Goeppert and G. K. S. Prakash, *ChemSusChem*, 2019, **12**, 3172.
59 R. K. Yadav, J. O. Lee, A. Kumar, N. J. Park, D. Yadav, J. Y. Kim and J. O. Baeg, *Sci. Rep.*, 2018, **8**, 1.
60 S. Chaubey, R. K. Yadav, S. K. Tripathi, B. C. Yadav, S. N. Singh and T. W. Kim, *Photochem. Photobiol.*, 2022, **98**, 150.
61 R. K. Yadav, G. H. Oh, N. J. Park, A. Kumar, K. J. Kong and J. O. Baeg, *J. Am. Chem. Soc.*, 2014, **136**, 16728.
62 R. K. Yadav, J.-O. Baeg, G. H. Oh, N.-J. Park, K. Kong, J. Kim, D. W. Hwang and S. K. Biswas, *J. Am. Chem. Soc.*, 2012, **134**, 11455.
63 S. Kumar, R. K. Yadav, K. Ram, A. Aguiar, J. Koh and A. J. F. N. Sobral, *J. CO2 Util.*, 2018, **27**, 107.
64 K. Kumar, R. K. Yadav, R. K. Verma, S. Singh, R. Shahin, R. Singhal, N. K. Gupta, C. Singh, D. K. Dwivedi and J. O. K. Baeg, *Catal. Sci. Technol.*, 2023, **13**, 5679.
65 N. Bano, I. Hussain, A. M. EL-Naggar and A. A. Albassam, *Appl. Phys. A: Mater. Sci. Process.*, 2019, **125**, 0.
66 A. Sotoudeh, G. Darbemamieh, V. Goodarzi, S. Shojaei and A. Asefnejad, *Eur. Polym. J.*, 2021, **152**, 110469.
67 M. Genedy, R. Chennareddy, E. M. Soliman, U. F. Kandil and M. M. R. Taha, *J. Reinf. Plast. Compos.*, 2017, **36**, 958.
68 R. K. Shukla, R. K. Yadav, V. L. Gole, C. Y. Na, G. H. Jeong, S. Singh, J. Baeg, M. Y. Choi, N. K. Gupta and T. W. Kim, *Photochem. Photobiol.*, 2023, **100**, 1235–1246.
69 M. Keramati, I. Ghasemi, M. Karrabi, H. Azizi and M. Sabzi, *Fibers Polym.*, 2016, **17**, 1062.
70 M. Dehghan and I. Sbarski, *Int. J. Chem. Nucl. Metall. Mater. Eng.*, 2014, **8**, 119.
71 H. Sun, B. Yu, J. Han, J. Kong, L. Meng and F. Zhu, *Polymer*, 2014, **38**, 477.
72 H. Norazlina and Y. Kamal, *Polym. Bull.*, 2021, **78**, 6911.
73 B. Subramanya and D. K. Bhat, *New J. Chem.*, 2015, **39**, 420.
74 K. Sharma, R. K. Yadav, S. Singh, C. Singh, R. Shahin, K. Kumar, R. K. Verma, D. K. Dwivedi, J.-O. Baeg and N. K. Gupta, *Mol. Catal.*, 2023, **548**, 113379.
75 S. Chaubey, P. Singh, C. Singh, S. Singh, S. Shreya, R. K. Yadav, S. Mishra, Y. Jeong, B. K. Biswas and T. W. Kim, *J. CO2 Util.*, 2022, **59**, 101968.
76 M. Gong, Q. Zhao, L. Dai, Y. Li and T. Jiang, *J. Asian Ceram. Soc.*, 2017, **5**, 160.
77 F. Ciftci, S. Ayan, N. Duygulu, Y. Yilmazer, Z. Karavelioglu, M. Vehapi, R. Cakır Koc, M. Sengor, H. Yılmazer, D. Ozcimen, O. Gunduz and C. B. Ustundag, *Int. J. Polym. Mater. Polym. Biomater.*, 2022, **71**, 898.
78 D. Akbar, F. Shabbir, A. Raza and N. B. Kahla, *Results Eng.*, 2025, **27**, 106291.
79 H. Belaid, S. Nagarajan, C. Teyssier, C. Barou, J. Barés, S. Balme, H. Garay, V. Huon, D. Cornu, V. Cavaillès and

M. Bechelany, *Mater. Sci. Eng. C*, 2020, 110, DOI: 10.1016/j.msec.2019.110595.
80 K. Kumar, R. K. Verma, J. Ramkumar and S. C. Jayswal, *Exp. Tech.*, 2025, **49**, 279–297.
81 K. Kumar, P. K. Kharwar and R. K. Verma, *E3S Web Conf.*, 2021, **309**, 01224.
82 D. K. Singh and R. K. Verma, *J. Thermoplast. Compos. Mater.*, 2022, **0**, 089270572211294.
83 Y. Ajaj, H. N. K. Al-Salman, A. M. Hussein, M. K. Jamee, S. Abdullaev, A. A. Omran, M. M. Karim, A. S. Abdulwahid and Z. H. Mahmoud, *et al.*, *Case Stud. Chem. Environ. Eng.*, 2024, **9**, 100612.
84 S. O. Han, M. Karevan, M. A. Bhuiyan, J. H. Park and K. Kalaitzidou, *J. Mater. Sci.*, 2012, **47**, 3535.
85 K. H. Dehnou, G. S. Norouzi and M. Majidipour, *RSC Adv.*, 2023, **13**, 3976.
86 D. K. K. Cavalcanti, M. D. Banea, J. S. S. Neto, R. A. A. Lima, L. F. M. da Silva and R. J. C. Carbas, *Composites, Part B*, 2019, **175**, 107149.
87 R. L. King, *Fibre-Reinforced Composites Materials, Manufacturing and Design*, 1989.
88 P. Szatkowski, L. Czechowski, J. Gralewski and M. Szatkowska, *Materials*, 2021, 14, DOI: 10.3390/ma14205955.
89 I. Taraghi, A. Fereidoon and A. Mohyeddin, *Steel Compos. Struct.*, 2014, **17**, 825.
90 D. K. Singh, R. K. Verma and S. Mishra, *J. Inorg. Organomet. Polym. Mater.*, 2023, **33**, 2954–2973.
91 M. Yuan, M. J. Kummer, R. D. Milton, T. Quah and S. D. Minteer, *ACS Catal.*, 2019, **9**, 5486.
92 C. F. Rosewall, P. A. Sibbald, D. V. Liskin and F. E. Michael, *J. Am. Chem. Soc.*, 2009, **131**, 9488.
93 H. Zheng, Z. Huang, P. Wei, Y. Lin, Y. Cao, X. Zhang, B. Zhou and C. Peng, *ACS Sustainable Chem. Eng.*, 2025, **13**, 4078–4092.
94 J. S. Lindsey and J. N. Woodford, *Inorg. Chem.*, 1995, **34**, 1063.
95 A. D. Adler, F. R. Longo, F. Kampas and J. Kim, *J. Inorg. Nucl. Chem.*, 1970, **32**, 2443.